Vibrations in materials with granularity

Zeravcic, Z.

CHAPTER 2

EXCITATIONS OF ELLIPSOID PACKINGS
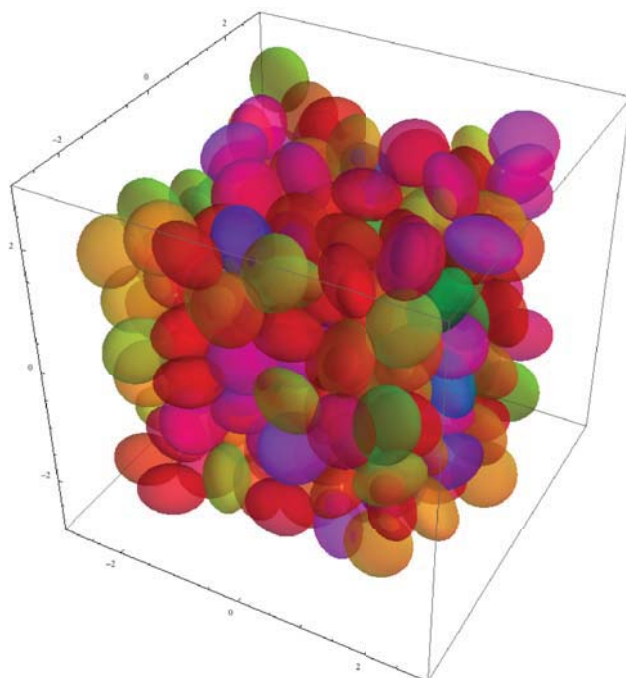
2.1   Introduction

As we introduced in general Introduction (Chapter 1), one of the most robust generic behaviors in all of materials science concerns the Density of States, *i.e.*, spectral density of vibrational excitations, $D(\omega)$. In a three-dimensional solid, the low-frequency spectrum should follow the Debye law $D(\omega) \sim \omega^2$ dictated by the elastic modes. However, this law breaks down for the case of a rigid solid formed from the jamming of spheres interacting via finite-ranged repulsions [7, 18, 28, 54, 55, 77, 78] (see Chapter 1, Section 1.2). The onset of jamming in such systems has features of a first-order transition, with a discontinuity in the number of interacting neighbors per particle [7, 37], as well as features of a second-order transition, with power-law scaling and diverging length scales [7, 18, 23, 28, 33, 37, 54, 55, 77, 79–83]. Just above the zero-temperature transition, $D(\omega)$ is approximately constant down to zero frequency [7, 18] implying the existence of a new class of low-frequency excitations that arise because the solid is on the edge of instability [28, 54, 55]. The Maxwell criterion for rigidity [84] (Section 1.2.3) proposes that the average number of interacting neighbors per particle, Z, should be high enough to constrain all relevant degrees of freedom in the sample: $Z \geq Z_{\mathrm{iso}}$. For frictionless spheres, the critical coordination number, $Z_{\mathrm{iso}} = 6$, *coincides* [7] with the value found at the jamming threshold packing fraction, ϕ_c (*i.e.*, $Z_c \equiv Z_{\mathrm{iso}}$). At packing fractions $\phi > \phi_c$, Z exceeds Z_{iso} and consequently the plateau in the density of states persists only down to a frequency ω^* that depends solely on $\delta Z = Z - Z_{\mathrm{iso}}$ [18, 28, 54, 55] (see Section 1.2.2). In small systems (like ones we study in this Chapter), an apparent gap emerges in the spectrum between $\omega = 0$ and $\omega = \omega^*$, while in large enough systems the "gap" is filled with ordinary elastic plane-waves described by Debye theory. The question that we want to address in this Chapter is whether the new physics of the excess modes is robust for jamming transitions generally [85] or whether it is applicable only to the idealized situation of spheres.

It was succinctly demonstrated [86] that in one sense spheres represent a singular situation and therefore may be a poor starting point for describing the generic properties of jammed solids. The introduction of even a small distortion to a sphere brings in many new degrees of freedom that need to be constrained for complete stability. While a sphere has only three relevant (translational) degrees of freedom, a spheroid (an ellipsoid with two equal axes) requires two additional coordinates to specify its orientation. Maxwell's counting argument, Section 1.2.3, for the rigidity of spheroid packings would necessitate an average coordination number $Z_{\mathrm{iso}} = 10$. This means that a discontinuous increase in density would be needed if the introduction of an arbitrarily small ellipticity required the average number of contacts per particle to jump discontinuously from 6 to 10. The rapid increase with ellipticity of the coordination number Z and, in particular, of the packing fraction [86–91] has garnered much attention ("M&M's pack more efficiently than spheres" [86, 87, 92]). Nevertheless, at the jamming threshold Z_c increases smoothly — not discontinuously — from $Z = 6$, as spheres deform into ellipsoids, so that for small ellipticity Z_c is *below* $Z_{\mathrm{iso}} = 10$ in apparent violation of the Maxwell criterion. While there are exactly the minimum number of contacts needed for mechanical stability at the jamming tran-

sition of spheres, there are fewer than the minimum number needed for ellipsoids. There must therefore be unconstrained degrees of freedom [89] so that the solid is not stable (to quadratic order) to some excitations. In this Chapter we investigate how rotational degrees of freedom introduce new non-zero-frequency excitations. In addition, we probe the nature of zero frequency modes. Remarkably, we find that these modes do not destroy the picture developed for spheres but instead can be naturally incorporated into this scenario.

This Chapter is organized as follows: First we are going to revisit in more detail Maxwell's counting argument for non-spherical particles. The following Section 2.3 will discuss the Gay-Berne potential used in our simulations. In Section 2.4 we are going to give more details about our packings and the methods we use to make them. Section 2.5 is devoted to the equations of motion and the derivation of the Dynamical Matrix. The rest of the Chapter is reserved for our results.

2.2 The Maxwell stability argument for spheroids and the occurrence of zero modes

It seems odd to think of Z_c as jumping discontinuously as soon as there is a minute distortion of the particles from spherical symmetry, so it is useful to briefly revisit Maxwell's argument for the stability/instability threshold [84] of spheroids (see Section 1.2.3). The minimum number of contacts necessary to clamp all particles which experience forces, Z_{iso}, is according to this argument twice the number of degrees of freedom of a particle. As the apparent discontinuity in Z_{iso} simply arises from our decision whether or not to include the rotational degrees of freedom in the counting, it is more intuitive to restore continuity by thinking of each sphere as having 6 degrees of freedom: three for translations and three for arbitrary rotations so that $Z_{\mathrm{iso}} = 12$. The rotations of individual (frictionless) spheres do not contribute in any way to the stability of the packing and are thus simply the $(Z_{\mathrm{iso}} - Z)/2 = 3$ zero-frequency modes per particle that are trivially localized on each particle. A natural scenario is that these innocuous zero-frequency modes progressively become mobilized into finite-frequency excitations with increasing ellipticity. There are clearly two important values of the coordination number, $Z_{\mathrm{spheres}} = 6$ and $Z_{\mathrm{iso}} = 12$. The important issue taken up here is the question: which of these controls the spectrum of excitations for the generalized case of ellipsoids?

From the above point of view, just above the jamming threshold, the fact that Z is below Z_{iso} should manifest itself in the presence of $(Z_{\mathrm{iso}} - Z)/2$ normal modes with zero frequency per particle — see Fig. 2.9. We study the nature of these modes and the question of how they become mobilized into finite-frequency excitations so as to find out whether this process changes the jamming scenario of frictionless spheres as the naive counting would suggest. We find that the above picture, in which the nontrivial vibrational/rotational modes are continuously turned on as the ellipticity is increased, unifies the scenario for aspherical particles with the one for spheres.

Since we are ignoring in the analysis below the trivial rotations about their symmetry axis, our spheroids (ellipsoids of revolution with one symmetry axis) actually have five rather than six nontrivial degrees of freedom. In this analysis, the critical contact number Z_{iso} is therefore 10 rather than 12 [86].

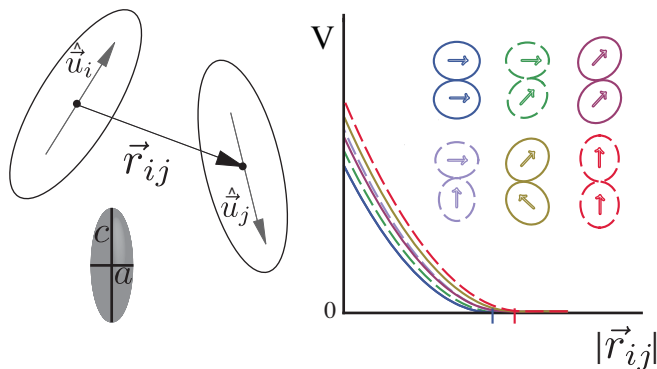## 2.3   Interaction potential: the Gay-Berne potential

Figure 2.1: An illustration of the Gay-Berne potential. Left: two Gay-Berne particles with their orientations and distance vector marked. Right: Gay-Berne harmonic potential, V, as a function of the separation of the particles $|\mathbf{r}_{ij}|$. Because of the nature of this potential (see main text for details), the relative orientation of the particles influences their interaction. Note that the lowest curve describes the situation in which ellipsoids are touching along their shorter axis (blue solid line), and the highest curve is for the case when the ellipsoids touch along their longer axis (red dashed line).

In our numerical study we simulate ellipsoids that are spheroidal: they have two principal axes a and b that are the same and a third one c that is different, $a = b \neq c$. Depending on the ratio of the axes, one distinguishes between oblate ellipsoids with $\varepsilon = c/a < 1$ ("M&M"s) and prolate ellipsoids with $\varepsilon = c/a > 1$ ("cigars").

The interaction of the ellipsoids is modeled by a modified Gay-Berne potential [93], which describes how two soft ellipsoids interact when they overlap. For two ellipsoids i and j, whose centers are located at $\mathbf{r}_i$ and $\mathbf{r}_j$, Fig. 2.1, the form of the potential is

$$V(r_{ij}, \sigma_{ij}) = \begin{cases} \frac{k}{\alpha}\left(\frac{\sigma_{ij} - r_{ij}}{\sigma_0}\right)^{\alpha}, & r_{ij} < \sigma_{ij}, \\ 0, & r_{ij} > \sigma_{ij}, \end{cases} \tag{2.1}$$

in terms of the distance between the centers of the ellipsoids $r_{ij} = |\mathbf{r}_j - \mathbf{r}_i|$ and the range parameter σ_{ij}. This expression is clearly the same as the power law potential which has been used in jamming studies of frictionless spheres [7]: when $r_{ij} = \sigma_{ij}$ the ellipsoids just touch and for $r_{ij} < \sigma_{ij}$ they repel with a force which is a power of the effective overlap $\sigma_{ij} - r_{ij}$. The orientation-dependent range parameter σ_{ij} is defined as

$$\sigma_{ij} = \sigma_0 \left[1 - \frac{\chi}{2} \left(\frac{(\hat{\mathbf{r}}_{ij} \cdot \hat{\mathbf{u}}_i + \hat{\mathbf{r}}_{ij} \cdot \hat{\mathbf{u}}_j)^2}{1 + \chi \hat{\mathbf{u}}_i \cdot \hat{\mathbf{u}}_j} + \frac{(\hat{\mathbf{r}}_{ij} \cdot \hat{\mathbf{u}}_i - \hat{\mathbf{r}}_{ij} \cdot \hat{\mathbf{u}}_j)^2}{1 - \chi \hat{\mathbf{u}}_i \cdot \hat{\mathbf{u}}_j} \right) \right]^{-1/2}, \tag{2.2}$$

Here, $\hat{\mathbf{u}}$ is a unit vector along the principal axis of the ellipsoid:

$$\hat{\mathbf{u}}_i = \sin\theta_i \cos\varphi_i \hat{\mathbf{x}} + \sin\theta_i \sin\varphi_i \hat{\mathbf{y}} + \cos\theta_i \hat{\mathbf{z}}. \tag{2.3}$$

By analyzing (2.2) in the two cases where $\hat{\mathbf{u}}_i$ and $\hat{\mathbf{u}}_j$ are parallel and perpendicular to each other, it is easy to see that $\sigma_0 = 2a = 2b$ and that the aspect ratio $\varepsilon = c/a$ of the particles is related to the dimensionless parameter χ by

$$\chi = \frac{\varepsilon^2 - 1}{\varepsilon^2 + 1}. \tag{2.4}$$

A plot of the Gay-Berne potential for various configurations of two contacting particles is shown in Fig. 2.1. Depending on how the particles are oriented upon making a contact, the potential between them differs (different curves in the plot).

The parameter k in the potential (2.1) sets the strength of the potential and plays the role of the bond stiffness for a one-sided repulsive harmonic potential ($\alpha = 2$ in (2.1)). For anisotropic particles, it is known as the well-depth anisotropy function and is typically taken to be a function of the three directions, $k = k(\hat{\mathbf{u}}_i, \hat{\mathbf{u}}_j, \hat{\mathbf{r}}_{ij})$. In order to simplify the expression for the potential, we take $k = 1$. This is a natural approximation for homogeneous particles with small $\delta\varepsilon$. Thus, for a one-sided harmonic potential (*i.e.*, $\alpha = 2$), the bond stiffness equals 1 for every contact.

2.4   Preparation of the packings and elimination of rattlers

Simulations were performed using N identical spheroids (equal size and mass m)[1]. The ellipsoids interact via the Gay-Berne potential described in Section 2.3. We studied both repulsive harmonic springs ($\alpha = 2$) and Hertzian interactions ($\alpha = 5/2$). Most simulations are done in a three-dimensional cubic box with periodic boundary conditions in all directions. Packings of spheroids were prepared by quenching random configurations at infinite temperature, $T = \infty$ to their local energy minima using conjugate gradient energy minimization [94]. In order to obtain a jammed packing at a desired $\delta\phi = \phi - \phi_c$, where ϕ_c is the packing fraction of the jamming transition at

---

[1]The code used to make the 3D packings was written by Prof. Ning Xu, one of the authors of the paper this Chapter is based on. This code was rewritten to produce 2D system by the author of this thesis.

fixed ε, we used the following protocol [18]. We first created a jammed configuration at a packing fraction just above $\phi_c(\varepsilon)$. To achieve that, we set a small energy tolerance per particle, say $\Delta E = 10^{-16}$ in units of kL^3, where L is the length of the system. If the energy per particle was larger than ΔE, the size of the spheroids was slightly decreased, and if the energy was smaller than ΔE, the size was increased. In doing so, the increment of change in the particle size was decreased progressively in order to eventually converge to a configuration with an energy per particle roughly equal to ΔE. This configuration was taken to be at the jamming threshold, so that its packing fraction was defined to be ϕ_c (this would be exactly true for $\Delta E = 0$). In order to obtain configurations at a given $\delta\phi$, the system was gradually compressed by repeatedly increasing the size of all particles slightly then quenching the system to its energy minimum, until the desired value of $\delta\phi$ was reached. The pressure was monitored during this process; a steady increase with packing fraction indicates an adiabatic change, but if the pressure was found to drop, indicating a significant rearrangement of the particles, the new corresponding ϕ_c was determined and the system was then gradually compressed from the new ϕ_c.

2D systems are generally easier to depict. Although all of the results we are going to show below are for the case of 3D ellipsoids, we will, however, often use 2D illustrations to emphasize some behavior. In Fig. 2.2 we are showing examples of packing with differing ellipticity, in 2D.

Note that for our typical tolerance for the energy of a particle, $\Delta E = 10^{-16}$, the tolerance for the overlap $\delta_{ij} = (\sigma_{ij} - r_{ij})/\sigma_0$ is of order 10^{-8} for one-sided harmonic springs, but only of order $4 \cdot 10^{-7}$ for Hertzian interactions. We suspect that this is the reason that the spread in our data of the average contact number Z (Fig. 2.10(a) below) is somewhat larger for Hertzian forces than it is for the harmonic springs.

We study two system sizes, $N = 216$ and $N = 512$, and average over about 100 independent initial configurations, at each value of Z and each density ϕ.

Rattlers (or floaters) were eliminated from the analysis as follows: in the first step, ellipsoids with fewer than $d + 1 = 4$ overlaps were removed. Since removal of a rattler could eliminate overlaps with particles that initially had 4 or more neighbors, we iteratively checked the number of overlaps and removed newly formed rattlers until all remaining ellipsoids had at least 4 interacting neighbors. If a particle had $\delta_{ij} = (\sigma_{ij} - r_{ij})/\sigma_0 < 10^{-8}$ for all of its overlaps (this rarely happens), it was also regarded as a rattler, *i.e.*, it was removed and the above procedure was repeated.

2.5   Equations of motion and dynamical matrix

In the following section we are going to derive the equations of motion that describe our system and find the dynamical matrix.

example packings
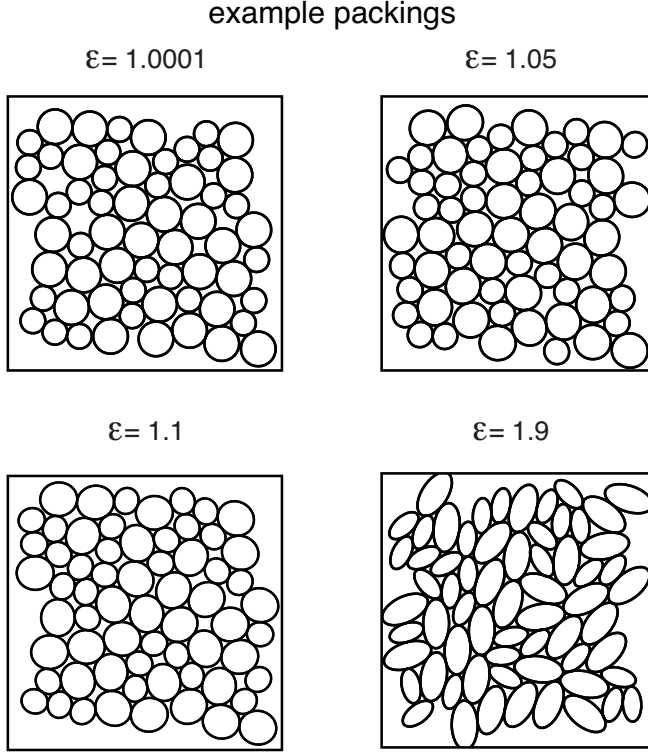
ε= 1.0001

ε= 1.05

ε= 1.1

ε= 1.9

Figure 2.2: Examples of 2D bidisperse packings with different ellipticities, for Harmonic interaction potential. These packings are at the onset of jamming. Even by eye, it is already clear that the density increases with increasing ε.

2.5.1   Equations of motion

The position of a rigid body is described by the coordinates of its center of mass, (x_i, y_i, z_i), and its orientation that is parametrized by the Euler angles $(\theta_i, \varphi_i, \psi_i)$. We used two coordinate systems — one is the lab system (X, Y, Z), and the other one is tied to the particle's center of mass (x_1, x_2, x_3), the so-called body system. For our ellipsoids we chose the x_3 axis along the vector $\hat{\vec{u}}$ (the vector along the $c-$axis of the ellipsoid).

In standard rigid body framework, if one considers a rotation of the body for a small angle, the angular velocity has a simple form:

$$\vec{\Omega} = \dot{\varphi}\vec{e}_Z + \dot{\theta}\vec{e}_N + \dot{\psi}\vec{e}_3,\tag{2.5}$$

where the $\vec{e}_N$ is the unit vector along the nodal line. In the body system it can be written as $\vec{e}_N = \cos\psi\vec{e}_1 - \sin\psi\vec{e}_2$. The components of the $\vec{e}_Z$ in the body system can be

found by applying the total rotational matrix (matrix that transforms the lab system into the body system) on a vector $(0,0,1)^T$. It is easy to show that the expression for the $\vec{e}_Z$ is then $\vec{e}_Z = \sin\psi\sin\theta\vec{e}_1 + \cos\psi\sin\theta\vec{e}_2 + \cos\theta\vec{e}_3$.

The expression for the angular velocity Ω can now be rewritten in the body system, with the following components:

$$\begin{cases} \Omega_1 = \dot\varphi(\vec{e}_Z)_1 + \dot\theta(\vec{e}_N)_1 \\ \Omega_2 = \dot\varphi(\vec{e}_Z)_2 + \dot\theta(\vec{e}_N)_2 \\ \Omega_3 = \dot\varphi(\vec{e}_Z)_3 + \dot\theta(\vec{e}_N)_3 + \dot\psi. \end{cases} \tag{2.6}$$

Working in the body system allows us to write the moment of inertia tensor in a diagonal form:

$$\hat{I} = \begin{pmatrix} I_1 & 0 & 0 \\ 0 & I_2 & 0 \\ 0 & 0 & I_3 \end{pmatrix}, \tag{2.7}$$

where I_1, I_2 and I_3 are principal moments of inertia. For our ellipsoids $I_1 = I_2 = I = m/5(a^2 + c^2)$ and $I_3 = 2m/5a^2$.

Now we have all the ingredients to write the equations of motion in the body system (the last three equations are known as Euler equations):

$$\begin{cases} m\ddot{x} = F_1 \\ m\ddot{y} = F_2 \\ m\ddot{z} = F_3 \\ I_1\dot\Omega_1 - (I_2 - I_3)\Omega_2\Omega_3 = K_1 \\ I_2\dot\Omega_2 - (I_3 - I_1)\Omega_3\Omega_1 = K_2 \\ I_3\dot\Omega_3 - (I_1 - I_2)\Omega_1\Omega_2 = K_3. \end{cases} \tag{2.8}$$

From considering the change of energy of the system due to an infinitesimal change of the particle's position and orientation:

$$\delta E = F_1 dx + F_2 dy + F_3 dz + K_Z d\varphi + K_N d\theta + K_3 d\psi, \tag{2.9}$$

we can see that the torque along the principal (rotational symmetry) axis of the ellipsoid K_3 has to be 0, since ψ describes a rotation around the rotational symmetry axis of the ellipsoid ($\vec{e}_3$), and thus does not change the energy, *i.e.*, $\partial E/\partial\psi = 0$. We can include this result into the Euler equations together with the fact that $I_1 = I_2 = I$, and the resulting equations are then:

$$\begin{cases} I\dot\Omega_1 - (I - I_3)\Omega_2\Omega_3 = K_1 \\ I\dot\Omega_2 - (I_3 - I)\Omega_3\Omega_1 = K_2 \\ I_3\dot\Omega_3 = K_3 = 0. \end{cases} \tag{2.10}$$

From the third Euler equation we have that $\dot\Omega_3 = 0$, *i.e.*, $\Omega_3 = const$ which we will take to be zero, because we don't have our ellipsoids rotating around their rotational

symmetry axis. If we again return to the Euler equations and include this, we will get even simpler expressions:

$$\begin{cases} I\dot{\Omega}_1 = K_1 \\ I\dot{\Omega}_2 = K_2 \\ \dot{\Omega}_3 = 0. \end{cases} \tag{2.11}$$

Before linearizing the equations of motion, we need to find the components of the force moment vector $\vec{K}$. We can write $\vec{K} = K_1\vec{e}_1 + K_2\vec{e}_2 + K_3\vec{e}_3 = K_Z\vec{e}_Z + K_N\vec{e}_N + K^*(\vec{e}_N \times \vec{e}_Z)$. Since we know the vectors $\vec{e}_Z$ and $\vec{e}_N$ in the body system, it is easy to show that the components of the force moment vector $\vec{K}$ are:

$$\begin{cases} K_1 = K_Z \sin\psi / \sin\theta + K_N \cos\psi \\ K_2 = K_Z \cos\psi / \sin\theta - K_N \sin\psi \\ K_3 = 0, \end{cases} \tag{2.12}$$

where we eliminated K^* by using $K^* = -K_Z \cos\theta / \sin\theta$, a result that comes out from the third equation.

We now proceed with the linearization of the equations of motion.

2.5.2 Linearization of the equations of motion

We are interested in the displacement of the ellipsoids around their equilibrium position. That means that $x \to x_0 + \delta x$, $y \to y_0 + \delta y$, $z \to z_0 + \delta z$, $\varphi \to \varphi_0 + \delta\varphi$, $\theta \to \theta_0 + \delta\theta$ and $\psi \to \psi_0 + \delta\psi$, where δ signifies a displacement. Since the variable ψ describes the rotation of an ellipsoid around its symmetry axis, it is justified to take the equilibrium value ψ_0 to be zero for each ellipsoid. Up to now we used a simplified notation by considering one particle. All the above equations should be written for all the particles in a packing, *i.e.*, we add an index i to all the variables.

The force moment vector $\vec{K}_i$ is in principle a function of the positions and orientations of all the particles. Since our energy (E) is actually the potential (V), which is a pair-potential between neighboring particles, in practice $\vec{K}_i$ will depend only on the coordinates of the neighboring particles. From a many particle version of equation (2.9) we see that the components of the vectors $\vec{K}_i$ are determined by the first derivatives of the potential with respect to the coordinates (*e.g.*, $K_{Z,i} = \partial V / \partial\varphi_i$). To linearize the equations we Taylor expand the components of the $\vec{K}_i$ and the $\vec{\Omega}_i$ up to linear order in the displacements. Since in equilibrium all the $\vec{K}_i$ are equal to zero, the lowest term in their expansion is already linear. The result of this expansion are the linear parts of the relevant quantities, and with taking into account that $\psi_{i,0} = 0$, they have the following form:

$$\begin{cases} \Omega_{i,1} = \delta\dot{\theta}_i \\ \Omega_{i,2} = \delta\dot{\varphi}_i \sin\theta_{i,0} \\ \Omega_{i,3} = 0 = \delta\dot{\varphi}_i \cos\theta_{i,0} + \delta\dot{\psi}_i \\ K_{i,1} = \delta K_{i,N} \\ K_{i,2} = \delta K_{i,Z}/\sin\theta_{i,0} \\ K_{i,3} = 0. \end{cases} \tag{2.13}$$

In the above we used the abbreviation δK for the linear part of K. More explicitly by using the Taylor formula we get:

$$\delta\vec{K}_i = \sum_{j=1,j\neq i}^{N} \frac{\partial\vec{K}_i}{\partial x_j}|_{eq}\delta x_j + \frac{\partial\vec{K}_i}{\partial y_j}|_{eq}\delta y_j + \frac{\partial\vec{K}_i}{\partial z_j}|_{eq}\delta z_j + \frac{\partial\vec{K}_i}{\partial\theta_j}|_{eq}\delta\theta_j + \frac{\partial\vec{K}_i}{\partial\varphi_j}|_{eq}\delta\varphi_j. \tag{2.14}$$

Finally we can write down the linearized equations of motion:

$$\begin{cases} m\delta\ddot{x}_i = \sum_{j\neq i} V''_{x_i x_j}\delta x_j + V''_{x_i y_j}\delta y_j + V''_{x_i z_j}\delta z_j + V''_{x_i\theta_j}\delta\theta_j + V''_{x_i\varphi_j}\delta\varphi_j \\\\ m\delta\ddot{y}_i = \sum_{j\neq i} V''_{y_i x_j}\delta x_j + V''_{y_i y_j}\delta y_j + V''_{y_i z_j}\delta z_j + V''_{y_i\theta_j}\delta\theta_j + V''_{y_i\varphi_j}\delta\varphi_j \\\\ m\delta\ddot{z}_i = \sum_{j\neq i} V''_{z_i x_j}\delta x_j + V''_{z_i y_j}\delta y_j + V''_{z_i z_j}\delta z_j + V''_{z_i\theta_j}\delta\theta_j + V''_{z_i\varphi_j}\delta\varphi_j \\\\ I\delta\ddot{\theta}_i = \sum_{j\neq i} V''_{\theta_i x_j}\delta x_j + V''_{\theta_i y_j}\delta y_j + V''_{\theta_i z_j}\delta z_j + V''_{\theta_i\theta_j}\delta\theta_j + V''_{\theta_i\varphi_j}\delta\varphi_j \\\\ I\sin^2\theta_{i,0}\delta\ddot{\varphi}_i = \sum_{j\neq i} V''_{\varphi_i x_j}\delta x_j + V''_{\varphi_i y_j}\delta y_j + V''_{\varphi_i z_j}\delta z_j + V''_{\varphi_i\theta_j}\delta\theta_j + V''_{\varphi_i\varphi_j}\delta\varphi_j. \end{cases} \tag{2.15}$$

Since the coordinate φ quantifies the rotations around the Z axis, the movement $\delta\varphi$ has to be weighed by the value of θ, hence the $\theta_{i,0}$ factor that appears in the fifth equation (*e.g.*, if $\theta_0 = 0$, $\delta\varphi$ is a rotation around the rotational symmetry axis, and so has no dynamics).

2.5.3 Dynamical matrix

In the usual case of vibrations, the terms on the right hand side of the dynamical equations, which are simply derivatives of the potential, determine the elements of the dynamical matrix D. In the absence of the angular terms, we can divide the first three equations of (2.15) through by m to get a symmetric dynamical equation D whose eigenvalues give the vibrational eigenfrequencies ω^2. However, in the presence of the angular degrees of freedom, the situation is slightly different [95], as we shall see below.

From the equations of motion it is straightforward to see what the elements of the dynamical matrix will be. But before we continue we need to rewrite our equations in such a way, that when we go to the Fourier domain we have an eigenvalue problem

(*i.e.*, on the left side of the equations we want only ω_i^2). This means that we have to rescale our coordinates — $|u_i^t\rangle \to \sqrt{m}\,|u_i^t\rangle$; $|u_i^r\rangle \to \sqrt{I}\,|u_i^r\rangle$. Since in our packings all the particles have mass $m = 1$, and the moment of inertia of the particles is the same for each particle, $I = 1/5a^2(1+\epsilon^2)$, this rescaling of the coordinates can be trivially done.

However, the equation for $\delta\varphi$ is still multiplied with a factor $\sin^2\theta_0^i$. This factor cannot be scaled out in the same manner as I and m factors, because it will make the matrix non-Hermitian. Since we are looking at a real system, the resulting appearance of the complex eigenvalues would indicate some sort of a damping in the system, that we don't have.

The solution to this problem is to solve the generalized eigenvalue problem : we have $|\hat{D} - \omega^2\hat{B}| = 0$, where $\hat{B}$ differs from the unit matrix by having elements $\sin^2\theta_0^i$ at the positions corresponding to the φ_i displacement. To obtain the eigenfrequencies ω^2, we solved the eigenvalue problem of the $\hat{B}^{-1}\hat{D}$ matrix. It can be shown (for a class of $\hat{B}$ matrices to which ours belongs) that, although the $\hat{B}^{-1}\hat{D}$ matrix is not Hermitian, the obtained spectrum must be real.

To calculate the diagonal 5×5 blocks of the dynamical matrix ("self-interaction"), we used expressions derived from imposing global translations and rotations as zero energy modes. Because of the periodic boundary conditions, these global rotations of the system are actually not eigenmodes of the system. This means that there are always at least 3 zero eigenmodes that correspond to the global translations of the system. Derived expression for the diagonal elements are:

$$
\begin{cases}
D_{ii}^{\alpha\beta} = -\sum_{j\neq i} D_{ij}^{\alpha\beta}, & \text{where } \alpha = x,y,z,\theta,\phi \text{ and } \beta = x,y,z \\[2em]
D_{ii}^{\alpha\theta} = -\dfrac{1}{J_i^{\theta\alpha}} \cdot \Bigg[-\dfrac{J_i^{\phi x}}{J_i^{\phi z}} \Bigg(\sum_{j\neq i} J_j^{\phi z} D_{ij}^{\alpha\phi} + \sum_j D_{ij}^{\alpha y} R_j^x - D_{ij}^{\alpha x} R_j^y \Bigg) \\[1.5em]
\quad + \sum_{j\neq i} J_j^{\theta x} D_{ij}^{\alpha\theta} + J_j^{\phi x} D_{ij}^{\alpha\phi} + \sum_j D_{ij}^{\alpha z} R_j^y - D_{ij}^{\alpha y} R_j^z \Bigg], \text{ where } \alpha = x,y,z,\theta,\phi \\[2em]
D_{ii}^{\alpha\phi} = -\dfrac{1}{J_i^{\phi z}} \Bigg(\sum_{j\neq i} J_j^{\phi z} D_{ij}^{\alpha\phi} + \sum_j D_{ij}^{\alpha y} R_j^x - D_{ij}^{\alpha x} R_j^y \Bigg), \text{ where } \alpha = x,y,z,\theta,\phi.
\end{cases} \quad (2.16)
$$

In previous equations $\hat{J}$ is the Jacobian that connects spherical θ and ϕ coordinates with x, y, z:

$$
\hat{J}_i = \begin{pmatrix} -\sin\phi_0^i & \cos\phi_0^i & 0 \\ -\cot\theta_0^i\cos\phi_0^i & -\cot\theta_0^i\sin\phi_0^i & 1 \end{pmatrix}, \quad (2.17)
$$

where the first row corresponds to θ and second row to ϕ coordinate.

2.5.4 Units and rescaling of the frequencies

We arbitrarily set the mass of the spheroids equal to 1. For the one-sided harmonic potential ($\alpha = 2$) and $k = 1$, the units are then the same in the limit $\varepsilon \to 1$ to the ones employed before in studies of the density of states, $D(\omega)$, of frictionless spheres [18]. Spatial scales are measured in units of $\sigma_0 = 2a = 2b$.

For Hertzian forces ($\alpha = 5/2$) the effective stiffness of the bonds becomes smaller as the jamming point is approached. Since the effective stiffness k_{eff} scales as $k_{\text{eff}}(\delta_{ij}) \simeq \delta^{1/2} \sim p^{1/3}$, where δ is the typical dimensionless overlap $(\sigma_{ij} - r_{ij})/\sigma_0$, and p is the pressure, the frequency scale goes down as $\delta^{1/4} \sim p^{1/6}$. In order to facilitate comparison with the results for one-sided harmonic springs, we therefore report, following [77], our results for Hertzian interaction in terms of scaled frequencies $\tilde{\omega} = \omega / p^{1/6} \simeq \omega / \sqrt{k_{\text{eff}}(\delta)}$.

2.6 Analysis

2.6.1 Continuous change of the average contact number Z and volume fraction ϕ

As was already mention in the Introduction of this Chapter, numerical work on hard ellipsoids and experimental work on M&M's [86, 87, 92] showed that both the average contact number Z and the volume fraction ϕ change continuously, when the ellipticity of the particles is changed from the spherical value $\varepsilon = 1$.

In Fig. 2.3 we are showing this behavior for our 3D system with soft ellipsoid harmonic interaction potential: In (b) we show the coordination number versus aspect ratio, $\varepsilon \equiv c/a$ of spheroids where c and a are the length along and the width perpendicular to the symmetry axis respectively. $\varepsilon < 1$ corresponds to oblate spheroids ("M&M's") and $\varepsilon > 1$ to prolate ones. The black symbols correspond to configurations evaluated very close to the jamming threshold $\phi_{\text{c}}(\varepsilon)$ for each value of ε. The other colors correspond to compressions $\delta\phi \equiv \phi - \phi_{\text{c}}$ relative to the threshold jamming density $\phi_{\text{c}}(\varepsilon)$. Note that Z depends both on ε and $\delta\phi$. The horizontal dashed line at $(Z-6) = 4$ corresponds to $Z_{\text{iso}} = 10$ which is the Maxwell criterion for rigidity of spheroids.

We have checked in all cases that the number of zero-frequency modes per particle at threshold is precisely $(Z_{\text{iso}} - Z)/2$; this is shown by the gray crosses. The inset shows that for both oblate and prolate spheroids at the threshold $\delta Z \equiv (Z - 6) = (6.6 \pm 0.3)|\delta\varepsilon|^{0.50 \pm 0.04}$, where $\delta\varepsilon \equiv \varepsilon - 1$, in agreement with results for two-dimensional ellipses [89, 96].

In Fig. 2.3(b) we show the change of the volume fraction ϕ with the change of $\delta\varepsilon$. The black symbols correspond to configurations at the onset of jamming, while the rest of the colored data is for compressed configurations. As in previous studies [86–92], ϕ has a maximum for some value of the ellipticity (for our configurations at the onset these values are $\phi \approx 0.7$ and $\delta\varepsilon \approx 1.5$), after which it starts to slowly decay.
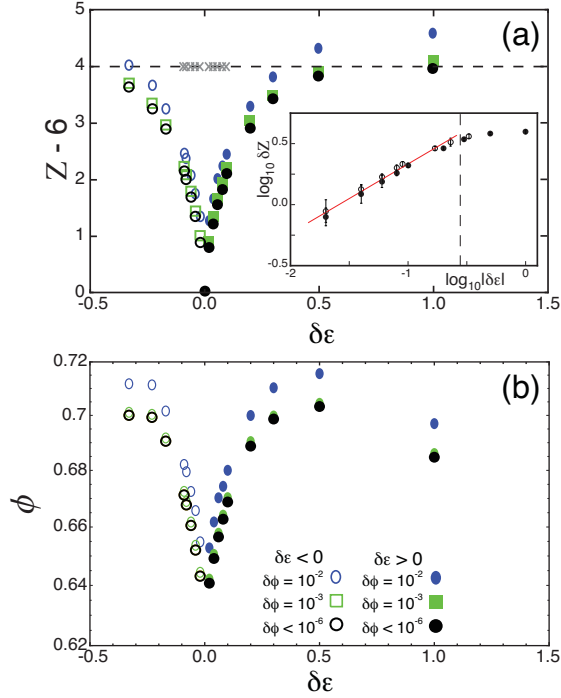
Figure 2.3: The average contact number Z and volume fraction ϕ, of harmonic packings. (a) Z as a function of the ellipticity $\delta\varepsilon \equiv \varepsilon - 1$ and distance from jamming $\delta\phi$ for our 216-particle packings. The sharp decrease around the spherical case $\delta\varepsilon = 0$ is consistent with earlier results [86, 90, 91] for hard ellipsoids and spherically capped rods. The log-log plot of δZ versus $|\delta\varepsilon|$ in the inset shows that the rise of Z at jamming is consistent with a $\delta Z \sim \sqrt{|\delta\varepsilon|}$ scaling. The crosses in the main plot for small values of $\delta\varepsilon$ show that twice the measured number of zero-frequency eigenmodes per particle plus $Z - 6$ add up precisely to 4. (b) ϕ as a function of the ellipticity. For some value of $\delta\varepsilon$, the volume fraction develops a maximum, which was observed in earlier studies as well [86, 90, 91].

2.6.2 Harmonic potential

In Fig. 2.4(a-d), we show the averaged density of states $D(\omega)$ for twelve typical situations. In Fig. 2.4(a), we show $D(\omega)$ for spheroids that are close to spheres, $\delta\varepsilon = -0.04$, for three different compressions: close to jamming at $\delta\phi < 10^{-6}$ (black line), at $\delta\phi = 10^{-3}$ (green line) and for relatively large compression, at $\delta\phi = 10^{-2}$ (blue line). We find that for small $\delta\varepsilon$, the system behaves nearly as if it was made from spheres but with a new "rotational" band of excitations. The plateau in the translational band
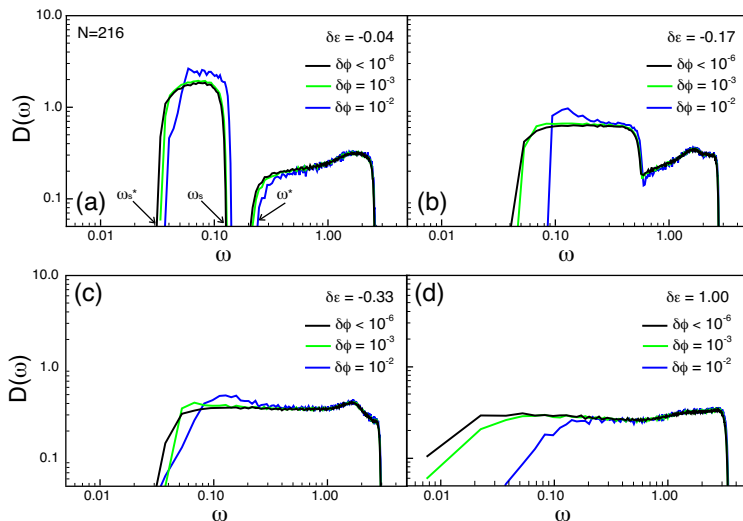
Figure 2.4: (a) The density of states for slightly oblate ellipsoids, $\delta\varepsilon = -0.04$, for our packings close to jamming and at two compressions. The existence of two bands separated by a gap as well as a gap at zero frequency is clearly visible. (b) For larger ellipticities the two bands merge, in our case for $\delta\varepsilon = -0.17$. Note how the different shapes of the merged bands are still visible. (c) As we continue to increase the aspect ratio of the particles, the separate shape of the bands vanishes, as illustrated here for $\delta\varepsilon = -0.33$. (d) Shows the data for $\delta\varepsilon = 1$ where $Z \approx Z_{\text{iso}} = 10$ at jamming. In accord with this, the gap near zero frequency increases with increasing compression (and therefore increasing Z). This is consistent with the argument that ω^* increases as Z increases above Z_{iso}.

of $D(\omega)$ still exists with a sharp onset, ω^*, determined by δZ. Our systems are too small to see the elastic plane-waves below ω^*. As we will show, ω^* scales in the same way as the plateau onset for spherical systems [18, 28, 54, 55]. The rotational band lies below the translational band and extends over the range $\omega_s^* \leq \omega \leq \omega_s < \omega^*$. As we will quantify, the spectrum is therefore described as having a lower-frequency rotational band separated by a gap from $\omega = 0$ as well as by a gap from a higher-frequency translational band.

As we increase ellipticity, at some value of $\delta\varepsilon$ the bands will merge, as can be seen in Fig. 2.4(b). The individual band shape is still visible, but the nature of the modes in the merged region will change, as we shall see in Section 2.6.2.

In Fig. 2.4(c), we show $D(\omega)$ for highly non-spherical particles, $\delta\varepsilon = -0.33$ for the same three values of compression as shown in Fig. 2.4(a). For these systems, the gap between the two bands has disappeared. In addition, when we compress packings for large ε which have $Z \approx Z_{\text{iso}}$ at jamming, a plateau of low-frequency modes appears.

Once we compress these packings that are at the isostatic point for ellipsoids, a gap opens up near $\omega = 0$, as shown in Fig. 2.4(d). This is in complete agreement with the scenario for spheres.

Nature of the new excitations

We can determine the nature of the excitations in the two bands by analyzing the eigenvectors of the dynamical matrix. We will do this only for the case of harmonic interaction potential. First we look at the relative contribution of the rotational degrees of freedom to the mode, $u_\mu(i)$, where $\mu = 1, 2, 3$ labels the translations and $\mu = 4, 5$ labels the two Euler coordinates of the orientation of each particle. In Fig. 2.5, we plot the rotational contribution:

$$\langle u_r^2 \rangle = \frac{\sum_{i=1}^N \sum_{\mu=4}^5 u_\mu^2(i)}{\sum_{i=1}^N \sum_{\mu=1}^5 u_\mu^2(i)} \tag{2.18}$$

and the translational contribution

$$\langle u_t^2 \rangle = \frac{\sum_{i=1}^N \sum_{\mu=1}^3 u_\mu^2(i)}{\sum_{i=1}^N \sum_{\mu=1}^5 u_\mu^2(i)} \tag{2.19}$$

separately. The lower band, existing below ω_s, is predominantly rotational in nature while the upper band, above ω^*, is translational. This is most pronounced when ε is small as shown in Fig. 2.5(a) and illustrated in (a1).

In the limit as ε approaches 0, we find that the contribution of $\langle u_r^2 \rangle$ in the upper band falls off as $(3.57(1) \cdot 10^{-4}) \, \omega^{-2.07(1)}$ up to the onset of localized modes at high frequencies. The scaling $\sim \omega^{-2}$ is precisely what one expects from perturbation theory if the rotational degrees of freedom are weakly coupled to the rotational ones. Fig. 2.5(b) shows the data at a larger ε where the bands have just merged. The now mixed character of modes is nicely captured by plots in Fig. 2.5(b1).

An illustration of how the purely rotational, translational and zero-frequency modes look like is shown in Fig. 2.6, for the 2D system.

Spectrum of ellipsoids — a different representation

Instead of binning the data so as to present them in terms of a density of states, we also give the individual frequencies as a function of mode number, obtained by averaging approximately 50 harmonic packings of 216 particles each, Figs. 2.7 and 2.8. The eigenvalues are ordered such that the frequency increases with increasing mode number.

Fig. 2.7(a) shows the frequencies on a log-log scale for $\delta\varepsilon = -0.17$. At this value of $\delta\varepsilon$, $Z \sim 8$ at the jamming transition density $\phi_c(\varepsilon)$, so that we expect about 1 zero mode per particle (about 216 in total). Due to our finite accuracy, these zero-frequency modes appear in Fig. 2.7(a) as the nearly flat set of points with frequencies of order 10^{-4} or less at the lowest $\delta\phi$. Note that these "zero-frequency modes" have $\omega^2 \approx 10^{-8}$,
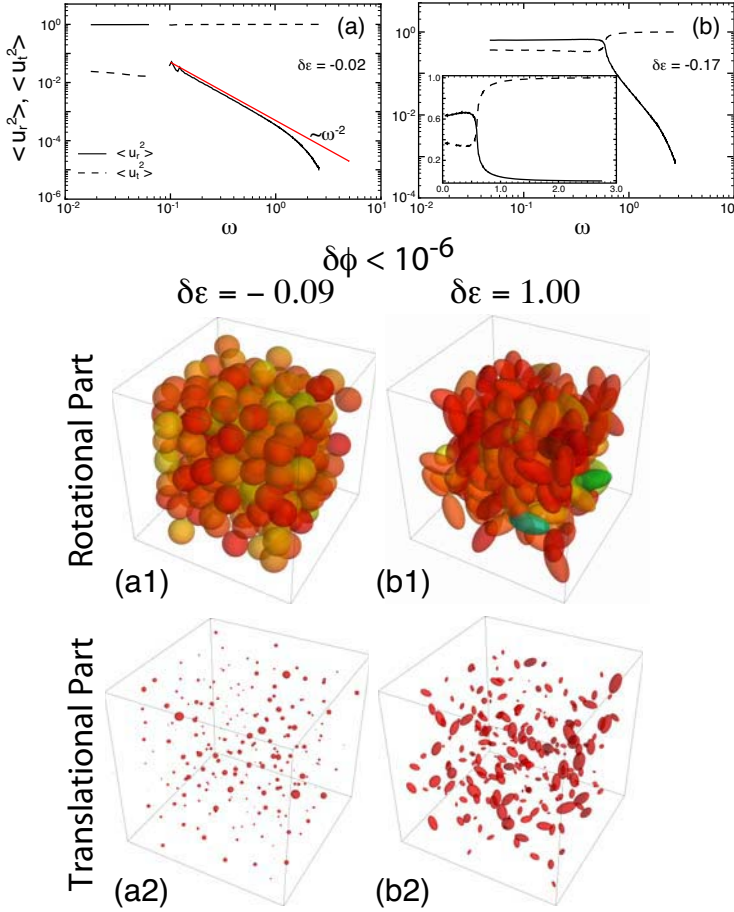
Figure 2.5: (a) Plot of the rotational component $\langle u_r^2 \rangle$ and the translational component $\langle u_t^2 \rangle$ of the eigenmodes for $\delta\varepsilon = -0.02$ as a function of ω. The lower frequency band is predominantly rotational, while the upper band is essentially translational. A predominantly rotational mode is illustrated in (a1). The red line indicates that at high frequencies the rotational contribution decreases as ω^{-2}. (b) The same as in (a), but with $\delta\varepsilon = -0.17$, when the gap between the two bands has just closed and most modes have mixed character. The inset of (b) show the same data in a linear scale. (b1) illustrates the character of a mixed mode at an even larger ellipticity.

which is consistent with the fact that we only determine typical forces in our packings to an accuracy of order 10^{-8} (see Subsection 2.4). The larger the slope in Fig. 2.7(a), the smaller the density of states, but the effect is not linear as it is distorted by the
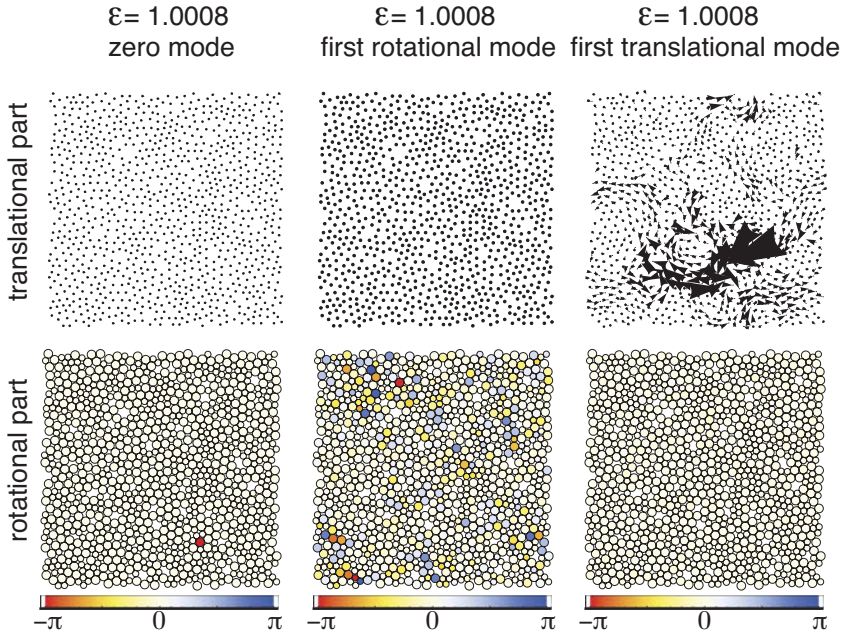
Figure 2.6: A purely translational, zero and rotational mode. Contributions of translations and rotations are plotted separately in the left and right column respectively. The size of the arrows corresponds to the amount of translational motion, whereas the color of the particles different than white indicates the amount of rotation of the particles. Note how for the case of zero modes, only one particle is rotating. The nature of the first rotational modes that appear in the spectrum is extended, as one can see in the lower middle plot.

logarithmic scale.

The kink in the curve at a frequency of order 0.6 marks the point where the rotational and translational bands merge, where $D(\omega)$ changes rapidly and the mixing between the bands is large. Fig. 2.7 shows the same type of data for slightly oblate ellipsoids, $\delta\varepsilon = -0.02$. In this case, the presence of a gap between $\omega \approx 0.05$ and 0.10 is clearly visible.

Fig. 2.8 shows eigenfrequencies ω versus mode number as a function of ε for a system of oblate ellipsoids, at a density close to jamming. The development of a gap and its shift with $\delta\varepsilon$ is again clearly visible. All the results stated in this Section are summarized in Fig. 2.9.
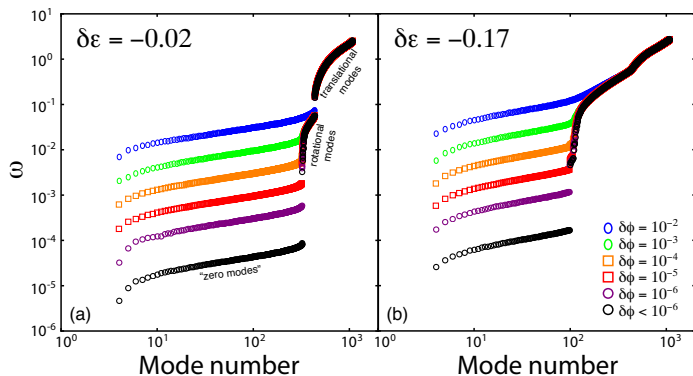
Figure 2.7: (b) Log-log plot of all the eigenfrequencies of our system vs. the mode number, for various densities at $\delta\varepsilon = -0.02$. The nearly horizontal set of data at low frequencies is again interpreted as zero-frequency modes. (b) Log-log plot of all the eigenfrequencies of our system vs. the mode number, for various densities at $\delta\varepsilon = -0.17$. The set of data at low frequencies, which forms a relatively flat curve, rapidly moves down upon approaching jamming. These data comprise, to within our numerical accuracy, the set of zero-frequency modes. A gap between the two bands at frequencies between about 0.05 and 0.10 is clearly visible.
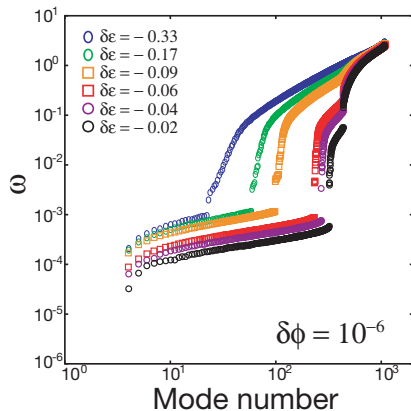

Figure 2.8: Log-log plot of all the eigenfrequencies of our system vs. mode number, for oblate particles of various ellipticities, at a density close to jamming, $\delta\phi = 10^{-6}$.
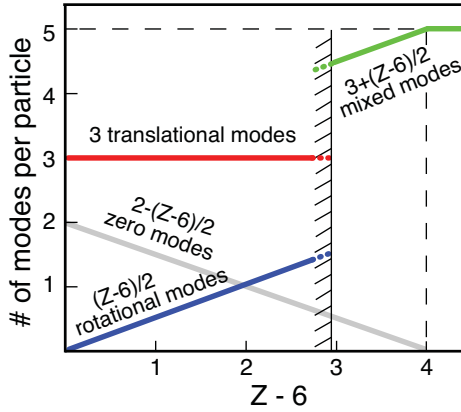
Figure 2.9: Illustration of how the number of different modes per particle (excluding rattlers) in the packings at jamming varies as a function of the average contact number Z. For $Z \lesssim 9$, there are two well-defined bands: a rotational band with $(Z-6)/2$ modes per particle and a translational band with three modes per interacting particle as is the case for spheres. Upon increasing Z, the number of zero modes decreases as zero-modes are converted into finite-frequency rotational modes. Above $Z \approx 9$, there is only one band.

2.6.3   Hertzian potential

In this subsection we present our results for Hertzian $N = 216$ particle packings, close to the jamming threshold. All the observed features and derived conclusions for the case of harmonic ellipsoid packings, described in the previous Subsection hold in the Hertzian case as well, as long as we scale all frequencies by the effective spring constant, k_{eff}, Subsection 2.5.4. Scaled frequencies are labeled as $\tilde{\omega}$ for Hertzian systems. The main difference lies in the increased statistical noise for the Hertzian packings, which is due to the different scaling of the interaction energy (for which the numerical tolerance is prescribed) with the particle overlaps, as is discussed at the end of the Subsection 2.4.

In Fig. 2.10(a) we plot the average excess of coordination δZ as a function of ellipticity for particles with Hertzian interactions. The statistical fluctuations inherent to our packings are very large for the smallest values of $\delta \varepsilon$, where we see a large deviation from the expected scaling $\delta Z \sim |\delta \varepsilon|^{0.5}$.

The density of states of our Hertzian packings shown in Fig. 2.10(b) is qualitatively consistent with our findings for the one-sided harmonic spring packings at small ellipticity, but the gap between the two bands is smaller and the scatter in the data is larger, as expected given the lower accuracy of the Hertzian data. We attribute the fact that the gap is smaller than for the harmonic packings to the fact that ω^* and ω_s
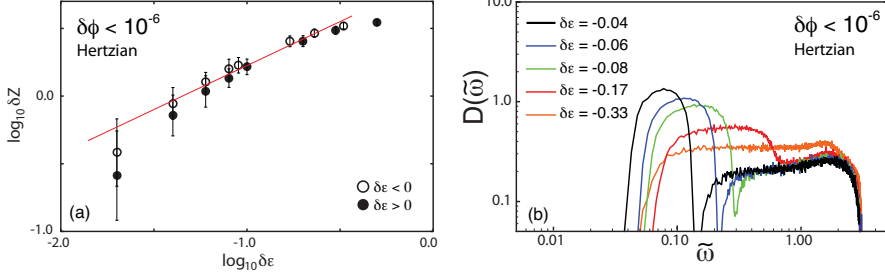
Figure 2.10: (a) Average excess contact number δZ vs. ellipticity $\delta\varepsilon \equiv \varepsilon - 1$ at the jamming threshold for packings of 216 (oblate - open symbols and prolate -closed symbols) ellipsoids interacting via a Hertzian interaction. The line has a slope of 0.65. (b) Density of states averaged over 100 Hertzian configurations, for five different ellipticities (oblate particles). Scaled frequencies are used, as explained in Subsection 2.5.4.

have, as we have seen, a different physical origin: ω^* is determined essentially by the excess coordination number δZ, irrespective of its origin, while ω_s depends on the form of the overlap potential and the ellipticity.

2.6.4   Participation ratio

To determine the homogeneity of the modes in space, we computed the participation ratio

$$P(\omega) = \frac{1}{N} \frac{\left(\sum_{i=1}^{N} u_{x,\mu}^2\right)^2}{\sum_{i=1}^{N} u_{x,\mu}^4} \tag{2.20}$$

of each mode. Fig. 2.11(a) shows that at low values of ε, the participation ratio is small and that for the highest frequencies near ω_s the modes become highly localized. Modes in the plateau of $P(\omega)$ for the rotational band are extended in nature. Since it is much easier to show this behavior for the 2D system, we simulated a packing with $\delta\varepsilon = 0.08$, where this extended nature is captured with all the particles rotating throughout the system. The two largest values of $\delta\varepsilon$ shown in (a) are the also shown in panel (b) of this figure, where on can see that they describe the case where the bands have just merged. We also extracted the value of the plateau of $P(\omega)$ for various ellipticities and system sizes, Fig. 2.11(c)[2]. Our data indicates that the plateau for the smallest ellipticities has a finite value, indicating extended nature of the modes. For sufficient ellipticities value of the plateau saturates to ≈ 0.3.

---

[2]Here we show only one system size, $N = 216$, but we have checked this behavior for $N = 512$ and $N = 1024$ as well
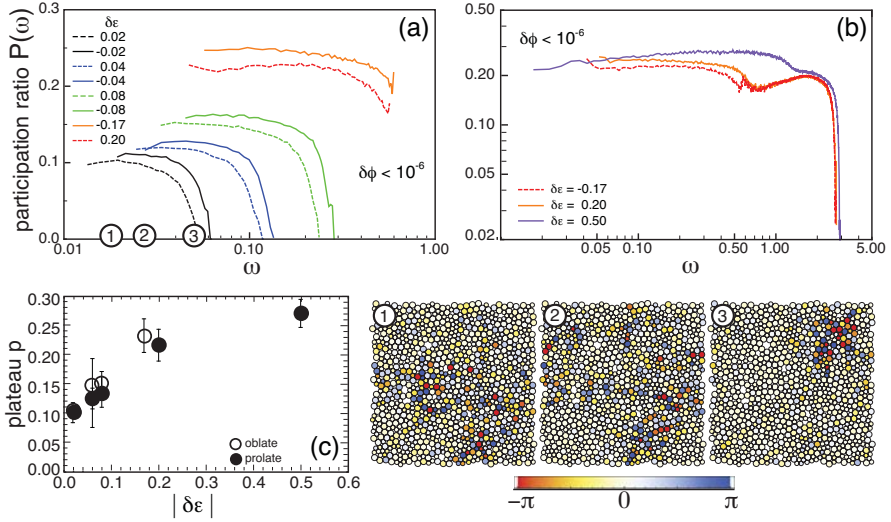
Figure 2.11: Participation ratio $P(\omega)$ of the rotational modes for various ε as a function of frequency. (a) The eigenmodes at the upper edge of the rotational band are seen to be strongly localized; throughout the rest of the band $P(\omega)$ is quite flat and rather small. The data at the largest ellipticities ($\delta\varepsilon = -0.17$, and 0.20) correspond to values where the gap between the two bands has just closed — the dip in these data is the vestige of the merging of the two bands. These two curves, together with the one for $\delta\varepsilon = 0.50$, are shown in panel (b), but now for the whole spectrum. In panel (c) we show the behavior of the plateau of the participation ratio with the increase of the aspect ratio of the particles. Mode plots marked with 1-3, are the 2D illustrations of the modes living in the plateau of $P(\omega)$, where one can see the extended behavior in our finite systems.

2.6.5 Scaling of the relevant frequencies

Harmonic potential

In Fig. 2.12(a) the frequency of the lower edge of the rotation band, ω_s^* is plotted vs. $|\delta\varepsilon| = |\varepsilon - 1|$. For small ε, the behavior is essentially linear; for large ε, when Z at jamming approaches 10, the gap closes. Fig. 2.12(b) shows ω_s and ω^* as functions of $|\delta\varepsilon|$ for harmonic configurations of prolate ellipsoids that are close to the jamming threshold. We find $\omega^* = (1.4 \pm 0.3)|\delta\varepsilon|^{0.6\pm0.1}$ and $\omega_s = (3.5 \pm 0.3)|\delta\varepsilon|^{1.1\pm0.1}$. The scaling of ω_s can be understood as the maximum frequency of a libration mode. As Fig. 2.11 shows, this mode is strongly localized, so we can obtain the scaling of the maximum frequency by estimating the torque response for rotating a single ellipsoid, keeping the other ones fixed. For a small rotation by an angle $d\theta$, a contact is compressed or decompressed by an amount $\sigma_0|\delta\varepsilon|d\theta$, where σ_0 is the size of the ellipsoids. This
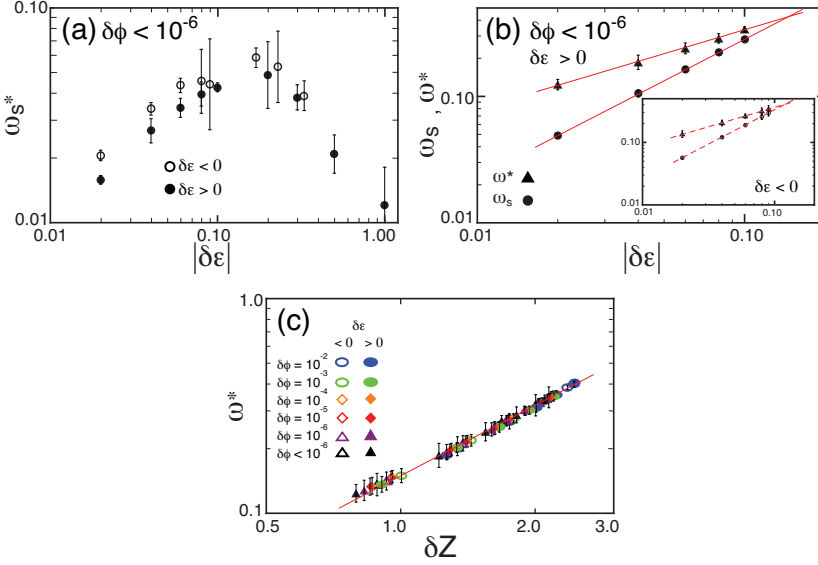
Figure 2.12: (a) Results for ω_s^*, the lower edge of the rotational band, as a function of ellipticity. For large ellipticities ω_s^* decreases as Z approaches 10 at jamming. (b) Scaling of ω_s and ω^* with $\delta\varepsilon$. Data is for prolate ellipsoids. ω_s, the frequency corresponding to the upper edge of the rotational band, which exists for small ellipticity, scales approximately linearly in $\delta\varepsilon$ at jamming, in agreement with the argument given in the text, while ω^* scales as $|\delta\varepsilon|^{0.6(1)}$ (the red lines are the best fits of the data). The point where the two lines cross marks the vanishing of the gap between the two bands. Inset: the same data for oblate ellipsoids. Numerically, the values are very close to those for prolate ellipsoids at the same ellipticity. (c) Scaling of ω^* for various compressions for oblate and prolate ellipsoids, showing that ω^* is determined by the contact number only, and that ω^* varies linearly in δZ, just as it does for spheres.

changes the normal force by an amount $k_{\text{eff}}\sigma_0|\delta\varepsilon|d\theta$, with k_{eff} the effective bond strength (which is constant for harmonic forces but density-dependent for Hertzian ones). For a slightly oblate or prolate ellipsoid, the change in torque is smaller by an amount $|\delta\varepsilon|$, hence of order $k_{\text{eff}}\sigma_0|\delta\varepsilon|^2 d\theta$ (for the harmonic data k_{eff} is 1). Since we scale out the factor $k_{\text{eff}}^{1/2}$ from our frequencies, this implies that the maximum scaled frequency $\omega_s \sim |\delta\varepsilon|$, independent of the force law (see the following Subsection for the results of the Hertzian packings). Similar results are found in two dimensions [96]. The inset of Fig. 2.12(b) shows ω_s and ω^* as functions of $|\delta\varepsilon|$ for oblate ellipsoids. Values of the exponents that we find for oblate ellipsoids are, within the error bars, the same as for prolate ones, with prefactors of ω_s and ω^* that are 10% and 15% higher, respectively.

In Fig. 2.12(c) we show ω^* as a function of δZ for different compressions and ellipticities. ω^* is still dependent solely on δZ and therefore the translational band does not depend on whether the increase in δZ occurs due to an increase in compression or an increase in the aspect ratio of the particles. For spheres, the onset of the translational band is determined by the excess number of contacts. Our results show that for ellipsoids, the same scenario applies, *irrespective of the origin of the excess contacts*. Note that the upper and lower limits of the rotational band, ω_s and ω_s^* do not obey this simple behavior but depend differently on ellipticity and compression [97].
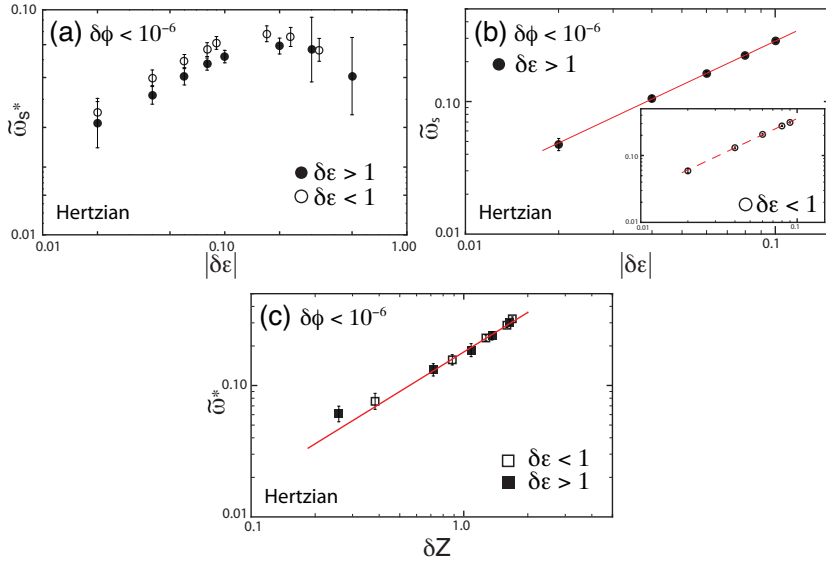

Figure 2.13: The characteristic (scaled) band frequencies versus ellipticity and coordination number for packings interacting via a Hertzian potential. (a) Lower edge $\tilde{\omega}_s^*$ of the rotational band as a function of ellipticity. (b) Scaling of the upper edge $\tilde{\omega}^s$ of the rotational band with ellipticity, for prolate ellipsoids. The line which is a guide to the eye has a slope of 1.1, the same value found for the harmonic packings. The inset shows the same data for oblate ellipsoids; the line has the same slope. (c) The dependence of $\tilde{\omega}^*$ on the excess number of contacts. The line has a slope of 1.

Hertzian potential

Fig. 2.13 shows the change in characteristic band frequencies, scaled as explained in Subsection 2.5.4, with ellipticity and coordination number for the case of particles interacting with a Hertzian potential. Again the observed scalings are quantitatively the same as for packings of harmonic ellipsoids.

2.6.6 Absence of elastic modes in our systems

In this study we have dealt exclusively with small systems, $N \leq 512$. This naturally raises the question about what finite-size effects are important.

In our finite systems, there is a gap below the frequency scale ω^*, which is defined as the low-frequency edge of the band of translational modes. For a sufficiently large system, the behavior is always elastic beyond scales ℓ^* [98]; hence there will always be elastic modes at frequencies below ω^*. In other words, the density of vibrational states will show Debye scaling, $D(\omega) \sim \omega^{d-1}$. Whether one observes elastic modes in a finite system depends therefore on the system size and the pressure or density (as the shear modulus depends on these). For large enough three-dimensional frictionless sphere packings, clear peaks in the $D(\omega)$ resulting from transverse elastic modes with $\omega = c_T k_n$ can indeed be seen [33]. However, the minimum frequency goes up as the system size decreases, since the minimum wave number of such modes is $k_{min} = 2\pi/L$ with L the linear system size. On the basis of Fig. 2.4 of [33], we estimate that the frequency of an elastic mode that occurs at our largest densities $\delta\phi$ is of order 0.3. Since ω^* is almost always smaller, in our relatively small systems the translational band appears gapped. As the jamming point is approached, the transverse elastic mode frequency becomes of course smaller, but since ω^* decreases with δZ faster than c_T, the translational band remains effectively gapped throughout the whole parameter range explored. Note that for large enough systems, plane-wave elastic modes will hybridize with the modes found in this study, so that localized rotational modes, for example, will become quasi-localized.

2.7 Conclusions and outlook

In conclusion, this study solves the problem of how the new degrees of freedom associated with non-spherical objects are incorporated into the normal-mode spectrum at the jamming threshold. Earlier findings [86–89] — that the isostatic conjecture breaks down for ellipsoid packings in the regime where $Z < 10$ — suggest that what happens for spheres does not immediately apply to more complex shapes. As a result, the packing problem of spheres has sometimes been viewed as an anomaly [86, 92]. If this would extend to the nature of the jammed state and its dynamic response, any perturbation from spherical symmetry would qualitatively change the character of marginally-jammed solid determined for spheres at Point J. Instead, we find that the structure of the normal-mode spectrum remains robust. The new modes that are introduced do not affect the plateau in the density of states until the spheroid ellipticity becomes large. Moreover, these rotational modes appear to be localized so that they should not be efficient at transporting heat. The onset of the modes in the translational band still depends only on the excess number of contacts $\delta Z = Z - 6$ as it does for spheres, irrespective of whether the excess contacts result from compression or particle asphericity. Thus, the singular jamming transition for spheres, Point J, in which the onset of jamming coincides with the isostatic point, controls the behavior

of systems of particles with more complex shapes, just as it controls the behavior of sphere packings that are compressed away from the transition.

There are two important regimes for ellipsoid packings: the first deals with small values of $|\delta\varepsilon| = |\varepsilon - 1|$ where the physics is a perturbation around the case of spheres; the second deals with large values of $|\delta\varepsilon|$, where $Z \to Z_{\text{iso}}$ (with $Z_{\text{iso}} = 10$ for spheroids and 12 for general triaxial ellipsoids). In the large $|\delta\varepsilon|$ case, the system is well described by a theory in which a plateau in the density of states opens up near zero frequency just as it did for the case of spheres near $Z = 6$. An interesting open question is how the gap closes when $Z \to 10$ for large ellipticities.

The insights we obtain from the present study are complementary to those obtained by including friction in the vibrational spectrum of a jammed solid [77]. Here we have a situation where the system jams when there are many fewer contacts than are needed according to the Maxwell rigidity criterion, while in the case of friction there is always an excess of contacts compared to the minimum necessary for stability [77, 83, 99–101]. Thus, in the case of friction there was never a question of a possible change in the underlying picture of the jamming threshold. Moreover, at the Coulomb threshold to mobilization, the response dictated by the friction law is inherently discontinuous, which makes the properties of packings with friction much more sensitive to the preparation history.

The addition of orientational degrees of freedom does introduce a new band that is essentially rotational in character while the upper band remains nearly completely translational. It is interesting to note that the low-frequency rotational modes couple in a simple manner to the higher-frequency translations. The boson peak seen ubiquitously in glasses has been ascribed [102] to the excess modes associated with the plateau of $D(\omega)$ — the fact that the jamming scenario is found to be so robust is crucial for its applicability to glasses.